Differential Nanoscale Topography and Functional Role of GluN2-NMDA Receptor Subtypes at Glutamatergic Synapses

Blanka Kellermayer, Joana Ferreira, Julien P Dupuis, Florian Levet, Dolors Grillo-Bosch, Lucie Bard, Jeanne Linarès-Loyez, Delphine Bouchet, Daniel Choquet, Dmitri Rusakov, et al.

The nanoscale topography of GluN2-NMDA receptor subtypes tunes plasticity at glutamatergic synapses

Blanka Kellermayer[1,2,3*], Joana S Ferreira[1,2*], Julien Dupuis[1,2*], Florian Levet[1-5§], Dolors Grillo-Bosch[1,2§], Lucie Bard[1,2,9§], Jeanne Linarès-Loyez[7,8], Delphine Bouchet[1,2], Daniel Choquet[1,2], Dmitri A. Rusakov[9], Pierre Bon[7,8], Jean-Baptiste Sibarita[1,2], Laurent Cognet[7,8], Matthieu Sainlos[1,2], Ana Luisa Carvalho[3,10], and Laurent Groc[1,2]

[1]Univ. de Bordeaux, Interdisciplinary Institute for Neuroscience, UMR 5297, F-33000 Bordeaux, France
[2]CNRS, IINS UMR 5297, Bordeaux, France
[3]CNC - Center for Neuroscience and Cell Biology, University of Coimbra, 3004-504 Coimbra, Portugal
[4]Univ. de Bordeaux, Bordeaux Imaging Center, F-33000 Bordeaux, France
[5]CNRS, Bordeaux Imaging Center UMS 3420, F-33000 Bordeaux, France
[6]INSERM, Bordeaux Imaging Center US 04, F-33000 Bordeaux, France
[7]Institut d'Optique & CNRS, LP2N UMR 5298, F-33400 Talence, France
[8]Univ. Bordeaux, Laboratoire Photonique Numérique et Nanosciences (LP2N), UMR 5298, F-33400 Talence, France.
[9]UCL Institute of Neurology, University College London, London, UK
[10]Department of Life Sciences, Faculty of Sciences and Technology, University of Coimbra, 3004-517 Coimbra, Portugal

[*, §]These authors equally contributed

Correspondence should be addressed to Laurent Groc (laurent.groc@u-bordeaux.fr) or Blanka Kellermayer (blanka.kellermayer@u-bordeaux.fr)

Short title: Nanoscale organization of synaptic NMDA receptors

Keywords: glutamate receptor, dSTORM, single molecule, GluN2 subunit, synapse

Highlights

- NMDAR are organized in nanodomains within hippocampal synapses
- GluN2A- and GluN2B-NMDAR are differentially organized at the nanoscale level
- GluN2A- and GluN2B-NMDAR nanodomains are regulated through different pathways
- GluN2A- and GluN2B-NMDAR relative ratio bi-directionally regulates LTP

eTOC

Kellermayer et al. describe the nanoscale organization of native NMDAR in developing hippocampal neurons. GluN2A- and GluN2B-NMDAR are organized in distinct nanodomains, which are differentially regulated by interaction with PDZ scaffolds. This GluN2A/2B nanoscale organization bi-directionally tunes synaptic LTP.

NMDA receptors (NMDAR) play key roles in the use-dependent adaptation of glutamatergic synapses underpinning memory formation in excitatory neuronal networks. In the forebrain, these plastic processes involve the varied contributions of GluN2A- and GluN2B-containing NMDAR that have different signaling properties. Although the molecular machinery of synaptic NMDAR trafficking has been under scrutiny over the last decades, the postsynaptic spatial organization of these two receptor subtypes, and its regulation, have remained elusive. Here, we used super-resolution imaging of NMDAR in rat hippocampal synapses to unveil the nanoscale topography of native GluN2A- and GluN2B-NMDAR. Both subtypes were found to be organized in separate nanodomains that, over the course of development, vary in number, area, shape, and localization. Furthermore, GluN2A- and GluN2B-NMDAR nanoscale organizations relied on distinct regulatory mechanisms. Strikingly, the selective rearrangement of GluN2A- and GluN2B-NMDAR, with no overall change in the NMDAR current amplitude, allowed bi-directional tuning of synaptic LTP. Thus, GluN2A- and GluN2B-NMDAR nanoscale organizations are differentially regulated and seem to involve distinct signaling complexes during synaptic adaptation.

INTRODUCTION

Glutamatergic synapses mediate most of the excitatory neurotransmission in the brain and adapt their strength to salient stimuli, often by involving the glutamate NMDA receptor (NMDAR) (Yashiro and Philpot, 2008). The role of NMDAR in the central nervous system has thus been extensively studied using genetic and pharmacological manipulations. NMDAR are heterotetramers comprising various combinations of GluN1, GluN2A-D, and GluN3A-B subunits that confer specific biophysical and pharmacological properties to the receptor (Paoletti et al., 2013), with GluN2A- and GluN2B-containing receptors being the predominant forms of NMDAR found in the forebrain. The relative content of GluN2A and GluN2B subunits directly influences long-term plasticity at forebrain synapses, and varies during brain development, sensory experience, and between brain hemispheres (Ito et al., 2000; Kawakami et al., 2003; Lau and Zukin, 2007; Smith et al., 2009; Yashiro and Philpot, 2008). Although it is well established that both receptor subtypes play important roles in synaptic adaptations, the specific involvement of GluN2A- and GluN2B-NMDAR in long-term potentiation (LTP) is still a matter of debate (Shipton and Paulsen, 2014; Yashiro and Philpot, 2008), which is likely attributable to the lack of appropriate pharmacological or genetic tools to finely dissect the GluN2A/2B contributions to NMDAR-mediated signaling (Bartlett et al., 2007; Berberich et al., 2005; Fox et al., 2006; Izumi et al., 2006; Li et al., 2007; Liu et al., 2004; Romberg et al., 2009). In addition, rapid modifications of the GluN2A/2B ratio occur shortly after the induction of synaptic potentiation in young hippocampal neurons through fast redistribution of surface receptors (Bellone and Nicoll, 2007; Dupuis et al., 2014; Matta et al., 2011), thus adding an additional layer of complexity in defining the exact role of GluN2 subunits in synaptic plasticity.

The synaptic content of GluN2A- and GluN2B-NMDAR is regulated by exocytosis, endocytosis and lateral diffusion processes (Bard and Groc, 2011; Lussier et al., 2015; Paoletti et al., 2013). Once at the synapse, the anchoring of GluN2A- and GluN2B-NMDAR greatly depends on their cytoplasmic C-terminal tails that contain motifs for protein-protein interaction and phosphorylation (Lussier et al., 2015). Although these mechanisms undoubtedly control the NMDAR synaptic content, distinct

scaffold proteins and protein kinases have been identified to act on either GluN2A- or GluN2B-NMDAR, opening the possibility for different regulatory pathways and complexes (Lussier et al., 2015). Electron microscopy studies have suggested that the distributions of GluN2A- and GluN2B-NMDAR in the postsynaptic compartment and their regulatory mechanisms are distinct (Park et al., 2008; Shinohara et al., 2008). However, the nanoscale organization of GluN2A- and GluN2B-NMDAR pools within the postsynaptic compartment and the underlying molecular regulatory machinery remain an enigma.

Recent advances in super-resolution fluorescence microscopy enable imaging individual membrane receptors with sub-diffraction resolution (Liu et al., 2015; Sahl et al., 2017; Zhuang, 2009). Among super-resolution approaches (Godin et al., 2014), the single-molecule localization microscopy (SMLM) techniques, such as direct stochastic optical reconstruction microscopy (dSTORM) (Heilemann et al., 2008), are effective tools to establish the molecular architecture of subcellular structures such as synapses. By determining the position of single fluorescent molecules with nanometer-scale precision, SMLM allows the nanoscale reconstruction of molecular assemblies. These approaches have been successfully applied to unveil the organization of neurotransmitter receptors in neuronal networks. In particular, the AMPA and $GABA_A$ receptors are organized in nanoscale domains in postsynaptic densities of excitatory and inhibitory synapses, respectively (MacGillavry et al., 2013; Nair et al., 2013; Pennacchietti et al., 2017; Specht et al., 2013). Functionally, it has been proposed that these nanodomains of neurotransmitter receptors and scaffold proteins are dynamically regulated and control synaptic transmission through the alignment of pre- and postsynaptic molecular complexes (Tang et al., 2016). Presynaptically-localized receptors and channels have also been investigated using super-resolution imaging, revealing the functional relevance of such nanoscale organizations (Dudok et al., 2015; Ehmann et al., 2014; Zhan et al., 2014). Here, we used SMLM imaging, single nanoparticle tracking, and electrophysiological recordings to investigate the dynamic nanoscale organization of native GluN2A- and GluN2B-NMDAR and its role in the adaptation of hippocampal synapses.

RESULTS

Nanoscopic topography of surface GluN1-, GluN2A- and GluN2B-NMDAR

In order to map all membrane NMDAR, the GluN1 subunit was labelled in live hippocampal neurons at day *in vitro* (DIV) 17 using an antibody directed against the extracellular N-terminus (Lu et al., 2017). Using conventional, diffraction-limited epifluorescence imaging, the classical distribution of GluN1-NMDAR clusters was observed along dendrites (**Figure 1A,** upper panels). In contrast, dSTORM super-resolution imaging revealed that GluN1-NMDAR clusters were composed of several adjacent nano-sized objects, which we chose to refer to as nanodomains (**Figure 1A,** lower panel). As NMDAR in hippocampal neurons contain GluN2A and/or GluN2B subunits, we then labelled live neurons at DIV 17 with specific custom-made antibodies directed against the extracellular N-termini of GluN2A or GluN2B subunit (**Figure S1**). Both GluN2A- and GluN2B-NMDAR were expressed on the neuronal surface (**Figure 1B, S2A**). Diffraction-limited epifluorescence images of surface GluN2A- or GluN2B-NMDAR revealed comparable distributions along dendrites, with indistinguishable GluN2A- and GluN2B-NMDAR clusters (**Figure 1B, S2A-C**). Quantitative dSTORM imaging was then used to unveil the nanoscopic distribution of surface GluN2A- and GluN2B-NMDAR clusters (**Figure 1B-C, S3**). Details on n number, number of cells and independent experiments and statistical P values can be found in Table S1. In contrast with diffraction-limited epifluorescence imaging, the nanoscale distributions of GluN2A- and GluN2B-NMDAR were different at first sight, with more nanodomains of GluN2A-NMDAR. We used three gold-standard quantification approaches to analyze and compare GluN2A- and GluN2B-NMDAR clusters (for details refer to STAR Methods). Density-based spatial clustering of applications with noise analysis (DBSCAN) was first used to characterize the clusters (**Figure 1D**) (Ester et al., 1996). The GluN2A-NMDAR nanoscale cluster area was found to be ~50% larger than that of GluN2B-NMDAR (**Figure 1E, S4A**), indicating that GluN2A- and GluN2B-NMDAR synaptic organizations are different. dSTORM images also revealed that these clusters were not uniform, but contained distinct nanodomains **(Figure 1F)**. In order to better characterize the intra-

cluster organization and overcome the limitation of DBSCAN when analyzing structures in close proximity, we used a wavelet-based segmentation method applied to the intensity-based images (Nair et al., 2013), to perform a precise morphometric analysis of the nanodomains, such as the area, the number per cluster and the shape (**Figure 1F,G**). The areas of GluN2A- and GluN2B-NMDAR nanodomains were similar (**Figure 1G, S4B**). However, the number of GluN2A-NMDAR nanodomains was twice as large as that of GluN2B-NMDAR (**Figure 1G, S4C**). Furthermore, GluN2B-NMDAR nanodomains tended to be more elongated than GluN2A-NMDAR ones as evaluated by the shape factor (**Figure S4D**). Thus, GluN2A- and GluN2B-NMDAR form nanodomains with subunit-specific characteristics. Additionally, this morphometric analysis approach confirmed the difference between GluN2A- and GluN2B-NMDAR clusters observed using the DBSCAN analysis (**Figure S4E**, GluN2A: n = 315 clusters from 16 cells in a total number of 6 experiments; GluN2B: n = 148 clusters from 14 cells in a total number of 7 experiments). Finally, we used a Voronoï tessellation analysis (SR-Tesseler; segmentation framework-based) to finely characterize nanodomains (**Figure 1H**) (Levet et al., 2015)**.** Consistent with the previous analysis methods, GluN2A-NMDAR cluster area was found to be 50% larger than that of GluN2B-NMDAR (**Figure 1I, S4F**, for both GluN2A and GluN2B: n = 91 clusters from 8 cells in a total number of 4 experiments). In addition, GluN2A- and GluN2B-NMDAR nanodomain areas were similar whereas their numbers were different (**Figure 1I, S4G-H**). We further validated these 2D quantifications by performing 3D-dSTORM imaging of both NMDAR subtypes using the SELFI method to achieve quasi-isotropic 3D resolution independently of optical aberrations induced by sample inhomogeneities (Bon et al., 2018), and confirmed that the nano-organizations of GluN2A- and GluN2B-NMDAR were different, especially in terms of the nanodomain number per cluster (**Figure S5**). Thus, both GluN2A- and GluN2B-NMDAR are differentially organized in surface clusters.

Although most surface NMDAR clusters are synaptic (**Figure S6**), we then specifically investigated the nanoscale organization of GluN2A- and GluN2B-NMDAR within glutamatergic synapses labelled with the postsynaptic marker PSD95. GluN2A-NMDAR clusters were more strongly co-localized with PSD95 than GluN2B-NMDAR (**Figure S7A-B**). When their synaptic organization was

compared at the nanoscale level, the number and area of synaptic (PSD95-positive) GluN2A-NMDAR nanodomains were found to be larger than that of GluN2B-NMDAR (**Figure S7C-G**), consistent with previous observations. Noteworthy, fewer GluN2A- and GluN2B-NMDAR nanodomains were found when comparing non-synaptic (immunonegative for PSD95) to synaptic clusters (nanodomain number: GluN2A, PSD95+: 5.6 ± 0.25, n=186; PSD95-: 3.4 ± 0.3, n=128 clusters; $p<0.001$; GluN2B, PSD95+: 2.9 ± 0.2, n=69; PSD95-: 1.7 ± 0.1, n=68 clusters; $p<0.001$). Collectively, these data indicate that GluN2A- and GluN2B-NMDAR clusters are organized in nanoscale objects that bear subtype-specific features, in particular at synaptic sites.

Comparative nanoscale organization of GluN2A- and GluN2B-NMDAR within a same synapse

The differential nanoscale organization of GluN2A- and GluN2B-NMDAR suggests that these subtypes are not confined into similar compartments, even though GluN2A and GluN2B clusters appear to fully overlap in diffraction-limited images (**Figure S8**). To test this assumption, we decided to label simultaneously GluN2A- and GluN2B-NMDAR within synaptic GluN1-NMDAR clusters (**Figure S6**). To this end, we co-expressed exogenous GluN2A-HA and GluN2B-flag, as well as GluN1-GFP to delineate NMDAR clusters within dendritic spines (**Figure 2A**). The nanoscale organization of GluN2A- and GluN2B-NMDAR within the same GluN1-NMDAR clusters was similar to the one described in distinct clusters (e.g. number of nanodomains per cluster: 2.814 ± 0.262 GluN2A-HA, 1.385 ± 0.167 GluN2B-Flag, Mann Whitney test $p<0.0001$, **Figure 2B**). Interestingly, most GluN2A- and GluN2B-NMDAR nanodomains did not overlap with each other (**Figure 2B, C**). Indeed, the colocalization between nanodomains, measured as the fraction of overlapping surface divided by the total surface of the nanodomains of each label, only ranged between 20-40% (**Figure 2D**). This suggests that only a limited fraction of receptor subtypes are intermixed. Finally, we used two-color stimulated emission depletion (STED) microscopy, a conceptually different super-resolution imaging technique, to further decipher the nanoscale organization of tagged GluN2A- and GluN2B-NMDAR in the same GluN1-NMDAR cluster. Two-color STED images confirmed a heterogeneous distribution of each receptor

subtype, and the larger area occupied by GluN2A-NMDAR clusters compared to GluN2B-NMDAR (**Figure S9A, B**). Furthermore, only 30% of GluN2A-NMDAR were found to overlap with GluN2B-NMDAR in a given cluster (**Figure S9C**). Collectively, these data demonstrate that, at a given synapse, GluN2A- and GluN2B-NMDAR nanoscale organizations are different, and their respective nanodomains do not overlap extensively.

Developmental changes in the nano-organization of GluN2A- and GluN2B-NMDAR

During brain development, the subunit composition of NMDAR changes (e.g. Barth and Malenka, 2001; Monyer et al., 1994). In rodents, GluN2B-NMDAR are highly expressed at immature synapses, whereas GluN2A-NMDAR synaptic levels increase progressively after birth. To understand the nanoscale maturation of GluN2A and GluN2B-NMDAR, we immunostained these receptor subtypes at different time points of cell culture maturation. First, we established the maturation profile of glutamatergic synapses (PSD95+) in our cultured hippocampal networks, confirming that synapse numbers increase significantly over two weeks in vitro and show a concomitant developmental switch in GluN2A/B subunit enrichment (**Figure S2**). Next, we labelled GluN2A- or GluN2B-NMDAR in live neurons at DIV 10, 17 or 24 to perform dSTORM imaging. Interestingly, GluN2A-NMDAR clusters underwent a major reorganization throughout development (**Figure 3A-F**). Indeed, all cluster parameters - including area, molecule numbers, and nanodomain area and numbers per cluster - were affected (**Figure 3A-F**), with a marked change at DIV 17, a developmental stage at which most glutamatergic synapses acquire the axon-spine morphology. On average, GluN2A-NMDAR cluster areas increased between DIV 10 and 17, then diminished at DIV 24 (**Figure 3B**). These changes were paralleled by changes in the molecule density per cluster (**Figure 3C**) as well as in the absolute number of molecules (**Table S2**). For GluN2B-NMDAR clusters, only subtle changes were observed during this period (**Figure 3A-F**). GluN2B-NMDAR cluster areas increased between DIV 10 to 17, then remaining stable over time (**Figure 3B**). The molecule density per GluN2B-NMDAR cluster and the absolute number of molecules (**Table S2**) were not correlated with this profile as it was highest at

immature states, decreasing during maturation (**Figure 3C**). When comparing both NMDAR subtypes over these developmental stages, the GluN2A-NMDAR cluster area was found to be initially larger at DIV 10 and 17 compared to GluN2B-NMDAR, but this difference did not persist at DIV 24 (**Figure 3B**). Thus, the maturation profiles of GluN2A- and GluN2B-NMDAR nanoscale organizations were different. When exploring the evolution of morphometric characteristics of GluN2A- and GluN2B-NMDAR nanodomains over this developmental period, a similar trend was observed. Although initially larger for GluN2B-NMDAR compared to GluN2A-NMDAR at DIV 10, the nanodomain areas of both NMDAR subtypes followed a comparable maturation profile peaking at DIV 17 (**Figure 3E**). No significant difference was later observed at DIV24. The number of nanodomains also increased at DIV 17 for GluN2A-NMDAR whereas for GluN2B-NMDAR it increased only at later stages (**Figure 3F**), although GluN2A-NMDAR clusters contained more nanodomains compared to GluN2B-NMDAR at all maturation stages.

Together, these data indicate that the nanoscale organization of GluN2A- and GluN2B-NMDAR is highly regulated throughout the *in vitro* maturation of hippocampal networks, and suggest the presence of distinct regulatory strategies for each receptor subtype.

PDZ scaffold differentially regulates NMDAR nanoscale organization

To directly test whether different cellular mechanisms regulate the nanoscale organization of GluN2A- and GluN2B-NMDAR, we probed each subtype by interfering with its synaptic anchoring (Lau and Zukin, 2007). The PDZ binding motif at the C-termini of GluN2A- and GluN2B-NMDAR is involved in interaction with MAGUKs and plays a critical role in the synaptic organization of NMDAR (Frank et al., 2016). Thus, we chose to selectively alter GluN2A or GluN2B interactions with PDZ scaffolds using divalent biomimetic competing ligands that were applied for tens of minutes only in order to avoid any potential long-term synaptic re-organizations (**Figure S10**) (Bard et al., 2010; Sainlos et al., 2011). Building up on previously described peptides derived from the GluN2A subunit (Bard et al., 2010), we also designed ligands that mimic the GluN2B C-terminal motifs. Compared to

the GluN2A-derived divalent ligands, the GluN2B-based divalent biomimetic peptides showed an improved capacity to bind PDZ domains clusters over their corresponding monovalent counterparts (**Figure S10-12**). To quantify the capacity of biomimetic divalent competitive ligands to destabilize subunits in live synapses, single nanoparticle (Quantum Dot) tracking of GluN2A or GluN2B subunits was performed in neurons acutely exposed to cell-permeant TAT-conjugated peptides. Consistent with previous studies (Bard et al., 2010; Sainlos et al., 2011), competitive ligands strongly, selectively, and similarly interfered with the binding of the C-terminal domain of either GluN2A or GluN2B subunit with PDZ scaffold proteins (**Figure 4A, B**). In the presence of TAT-$2A_2$ ligands, the cluster area and molecule number of GluN2A-NMDAR were decreased significantly (**Figure 4C, Table S2).** As the nanodomain area and number remained stable (**Figure 4D**), the relative density of GluN2A-NMDAR within nanodomains significantly decreased (**Figure S13A**). In this condition, a slight but significant change in the GluN2B-NMDAR nanoscale organization was observed, i.e. an increased number of nanodomains (**Figure S14A-D**). Thus, when the interaction between GluN2A-NMDAR and PDZ scaffolds is artificially disrupted, GluN2A-NMDAR nanodomains are partially depleted in receptors while their geometry remains stable, and a mild simultaneous redistribution of GluN2B-NMDAR is observed.

Surprisingly, when GluN2B-NMDAR were challenged with TAT-$2B_2$ ligands, their nanoscale cluster area and molecule number were unaltered (**Figure 4E, Table S2**). Instead, the area of nanodomains significantly increased (**Figure 4F**), leading to a decrease in receptor density within nanodomains (**Figure S13B**). In parallel, a slight - but significant - change in the GluN2A-NMDAR nanoscale organization was observed (**Figure S14E-H**). Thus, disrupting the interaction between GluN2B-NMDAR and PDZ scaffolds triggers their redistribution within the synapse, promoting a reorganization of nanodomains without affecting receptor numbers. Together, these data demonstrate that GluN2A- and GluN2B-NMDAR are differentially regulated by the binding to PDZ scaffold. The regulation of GluN2A-NMDAR would thus involve changes in the receptor pool within

stably-defined nanodomains, whereas the regulation of GluN2B-NMDAR involves changes in the nanodomain topography with a rather stable receptor pool.

GluN2A- and GluN2B-NMDAR nanoscale redistributions tune synaptic LTP

The observation that GluN2A- and GluN2B-NMDAR nanoscale organizations are distinct and differentially regulated by scaffold partners raises the possibility that these nanodomains are involved in different physiological functions. Earlier studies have revealed that both GluN2A- and GluN2B-subunit containing NMDAR are involved in long-term synaptic plasticity (Shipton and Paulsen, 2014; Yashiro and Philpot, 2008). However, the respective contribution of each receptor subtype to synaptic LTP is still hotly disputed, mainly because of the limitations inherent to the antagonist- or knock-out-based approaches involved. To circumvent this, we took advantage of the biomimetic competing ligands described above aiming to selectively disorganize either GluN2A- or GluN2B-NMDAR synaptic nanodomains, and to see how this affects LTP expression.

First, we examined the relative synaptic content of GluN2A- and GluN2B-NMDAR by recording NMDAR-mediated EPSCs at CA3-CA1 glutamatergic synapses in presence of either NS_2, $2A_2$, or $2B_2$ ligands infused through the patch pipette, while delivering bath applications of the GluN2A- or the GluN2B-selective antagonists Zn^{2+} (250 nM) and Ro 25-6981 (2 µM), respectively (**Figure 5**). In the absence of biomimetic peptide or in the presence of the control NS_2 ligand, a significant decrease in NMDAR EPSC amplitude was observed in presence of Ro 25-6981 (by 27% or 32%, respectively; **Figure 5A-C**). This reflected the basal GluN2B-NMDAR contribution to NMDAR-mediated synaptic currents. Conversely, partial GluN2A blockade through Zn^{2+} (250 nM) application inhibited NMDAR-mediated EPSCs by 41% in the absence of peptide and by 36% in the presence of the control NS_2 ligand (**Figure 5D-F**). In comparison, $2A_2$ ligand infusion enhanced the Ro 25-6981-dependent inhibition of NMDAR EPSC by up to 43% and decreased Zn^{2+}-dependent NMDAR blockade down to 16%, consistent with a lateral escape of synaptic GluN2A-NMDAR and relative enrichment in GluN2B-NMDAR (**Figure 5A-F**). When infusing the $2B_2$ ligand, Ro 25-6981-dependent inhibition of NMDAR EPSC significantly

decreased down to 12% while Zn^{2+}-dependent blockade increased up to 60%, consistent with a synaptic depletion of GluN2B-NMDAR and a relative enrichment in GluN2A-NMDAR (**Figure 5A-F**). Interestingly, these manipulations only altered the relative abundance of GluN2A- and GluN2B-NMDAR as the overall amount of synaptic NMDAR remained stable. Indeed, the amplitude of NMDAR EPSCs at CA3-CA1 glutamatergic synapses was unchanged during the exposure to either NS_2, $2A_2$, or $2B_2$ ligands (**Figure 5G,H**), consistent with earlier observations in cultured hippocampal neurons (Bard et al., 2010). Thus, these competing ligands alter the receptor nanoscale organization and GluN2A/2B synaptic ratio (20-40%), but leave the overall amplitude of NMDAR-mediated currents intact.

We next tested the role of GluN2A- and GluN2B-NMDAR relative organization in the ability of CA3-CA1 synapses to express LTP. A standard LTP-induction protocol with NS_2 control ligands infused whole-cell produced a persistent 214% potentiation that could be fully blocked by the bath application of the NMDAR competitive antagonist AP5 (50 µM) (**Figure 6A-C**). Strikingly, whole-cell dialysis of $2A_2$ increased the magnitude of LTP (measured 40 min after induction) by 64% when compared to the control NS_2 ligand infusion condition (**Figure 6A-C**). In contrast, $2B_2$ dialysis decreased the magnitude of LTP by 86% when compared to the NS_2 condition (**Figure 6A-C**). Collectively, these data suggest that the acute manipulation of the GluN2A/GluN2B-NMDAR synaptic ratio, while having no effect on the overall NMDAR-mediated synaptic current, bi-directionally controls the range of use-dependent plasticity at CA3-CA1 hippocampal synapses: depleting synapses in GluN2A-NMDAR strengthens LTP expression whereas increasing the contribution of GluN2A-NMDAR weakens it.

DISCUSSION

Here, we used SMLM imaging and patch-clamp electrophysiology in hippocampal neurons to reveal the nanoscale organization of GluN2A- and GluN2B-NMDAR and its functional role in synaptic plasticity. Documenting the distribution of individual molecules revealed substantial differences between the nanoscale structures of the two NMDAR subtypes, particularly in the number, area, and shape of their nanodomains. At a given synapse, only a fraction of GluN2A- and GluN2B-NMDAR nanodomains overlap, indicating the presence of distinct regulatory macromolecular complexes that differentially evolve during development. Remarkably, acute exogenous re-organization of GluN2A- and GluN2B-NMDAR, which leaves intact the overall NMDAR-mediated current, bi-directionally tunes synaptic LTP (**Figure 6D**). Thus, the nanoscale organizations of membrane GluN2A- and GluN2B-NMDAR in hippocampal neurons are structurally different, regulated through distinct cellular mechanisms, and have contrasted consequences on the plastic range of synapses.

Advances in super-resolution microscopy have revealed that the nanoscale organization of neurotransmitter receptors, scaffolds, and signaling molecules is structured in the postsynaptic compartment (Broadhead et al., 2016; Frost et al., 2010; MacGillavry et al., 2013; Nair et al., 2013). For instance, in hippocampal synapses, AMPA receptors and PSD95 are clustered in 1-4 nanodomains (~50-80 nm size) that have been proposed to be plastic entities (MacGillavry et al., 2013; Nair et al., 2013). A subtype specificity in the nanoscale distribution of surface and intracellular GluN2A/2B-NMDAR was previously suggested based on the differential enrichment in PSD95 clusters (MacGillavry et al., 2013). Here, we provide the first surface mapping of both GluN2A- and GluN2B-NMDAR at the nanoscale level, revealing the presence of approximately 5-10 nanodomains (~55 nm) per synaptic area. The similarities between AMPA receptors, PSD95, and now NMDAR nanodomains in hippocampal synapses strengthen the view that the postsynaptic region is a highly compartmentalized entity. Interestingly, nanoclusters have also been identified with respect to other, non-neuronal membrane proteins (Garcia-Parajo et al., 2014). Therefore, nanoclustering appears to be a dominant feature of

membrane protein organization which potentially represents a mode of spatiotemporal orchestration of biochemical reactions as suggested by liquid-liquid phase transitions (Li et al., 2012). Compartmentalization is even more critical for the postsynaptic terminal in which it can accelerate reaction kinetics for signal transmission, as for PSD95 and SynGAP (Zeng et al., 2016). The postsynaptic receptor nanodomains are likely to boost neurotransmitter signals as they are spatially juxtaposed to the presynaptic release machinery (Tang et al., 2016). The differential and largely non-overlapping nanoscale organization of GluN2A- and GluN2B-NMDAR described here thus suggests the presence of distinct NMDAR-mediated transmission units. Furthermore, our data indicate that, if present, the GluN2A/2B tri-heterotetramers (Al-Hallaq et al., 2007; Gray et al., 2011; Rauner and Kohr, 2011) could represent up to 30% of postsynaptic NMDAR. Thus, NMDAR signaling may proceed from a nanoscale mosaic of GluN2A- and GluN2B-NMDAR complexes that could constitute, or be part of, distinct functional units in the synapse.

Over the past few decades, the mechanisms underlying the trafficking and synaptic anchoring of GluN2A- and GluN2B-NMDAR have been the subject of intense investigations. It has been proposed that the binding of GluN2A/B subunits to different MAGUK proteins, through the interaction between the C-terminus of GluN2A/2B subunits and PDZ domain of MAGUKs, plays an important role in their synaptic anchoring (Horak et al., 2014; Lussier et al., 2015). Here, surface GluN2A- and GluN2B-NMDAR were acutely challenged by altering scaffold binding, and their surface reorganization was monitored at the single molecule and nanoscale levels. Not surprisingly, the organization of both GluN2A- and GluN2B-NMDAR was altered by these molecular challenges, which was consistent with the role of PDZ scaffolds in the regulation of NMDAR-mediated transmission (Horak et al., 2014; Lussier et al., 2015). However, these modifications differed depending on the receptor subtype considered. Preventing the interaction between GluN2A-NMDAR and PDZ scaffolds - as measured in synapses and with ligand assays - reduced the number of receptors while preserving stable nanodomain topography. In contrast, disrupting the interaction between GluN2B-NMDAR and PDZ scaffolds did not alter receptor

numbers but instead affected the topography of nanodomains. These observations lend support to a model in which synapses would control GluN2A-NMDAR signaling by changing their number in defined stable domains, and GluN2B-NMDAR signaling by changing their topological organization. One prediction for GluN2B-NMDAR re-distribution is that once their anchoring with PDZ scaffold is disrupted, other mechanism(s) ensure their synaptic retention in different compartment(s). Furthermore, our data suggest that GluN2A- and GluN2B-NMDAR are in distinct complexes and/or domains. Consistent with these observations, NMDAR have been proposed to be partitioned into two discrete populations *in vivo*, which are referred to as 0.8 and 1.5 MDa NMDAR complexes that contain different subunit amounts and receptor combinations (Frank et al., 2016). In addition, GluN2A- and GluN2B-NMDAR do not play the same role in these complexes as the disruption of the interaction between GluN2B-NMDAR and MAGUK proteins dismantle NMDAR supercomplexes specifically (1.5 MDa). The GluN2A and GluN2B-NMDAR are thus likely to be specifically embedded into distinct nanoscale complexes, with different signaling cascade(s) and function(s).

What is the functional significance of this subunit-specific nanoscale organization of synaptic NMDA receptors? GluN2A- and GluN2B-NMDAR have been shown to differentially influence brain development, plasticity and sensory experience processes (Lau and Zukin, 2007; Paoletti et al., 2013). However, defining the respective roles of each receptor subtype in synaptic potentiation has remained a controversial issue, with the somewhat contrasting conclusions originating from antagonist- or knock-out-based studies addressing this question. Indeed, pharmacological or genetic interventions on either subunits had a varying impact on NMDAR-dependent LTP expression depending on the age and brain region (Shipton and Paulsen, 2014; Volianskis et al., 2015). Using divalent biomimetic ligands selectively acting on the synaptic content and nano-organization of GluN2A- or GluN2B-NMDAR, we show here that the GluN2A/2B ratio bi-directionally controls LTP at CA3-CA1 hippocampal synapses. Indeed, the $2A_2$ and $2B_2$ ligand infusions resulted in significant and selective up- and down-regulations of GluN2A- and GluN2B-NMDAR contributions, respectively,

while leaving NMDAR current amplitudes intact, suggesting that compensatory mechanisms allow for the maintenance of NMDAR synaptic homeostasis and that GluN2A- and GluN2B-NMDAR synaptic stabilization involve, for part, distinct scaffolding partners, as previously suggested (Lussier et al., 2015). Furthermore, our data demonstrate that a decrease in GluN2A/2B synaptic ratio at CA3-CA1 synapses boosts LTP expression whereas an increase suppresses it. Indeed, partial depletion of GluN2A-NMDAR at synapses extends the ability to express LTP whereas decreasing the contribution of GluN2B-NMDAR represses it, as previously suggested (Gardoni et al., 2009). The prominent role of GluN2B-NMDAR in synaptic potentiation could result from their unique ability to interact with and act as a cargo for CaMKII, allowing its fast redistribution and accumulation to dendritic spines where its activation by calcium influx triggers the induction and maintenance of synaptic potentiation (Bayer et al., 2001; Dupuis et al., 2014; Lisman et al., 2012; Otmakhov et al., 2004). As a consequence, preventing GluN2B-NMDAR synaptic stabilization may interfere with the CaMKII recruitment to dendritic spines and therefore impair LTP expression. Thus, GluN2A- and GluN2B-NMDAR could come as a twofold blow, with GluN2A-NMDAR acting as ionotropic calcium providers while GluN2B-NMDAR provide structural scaffolding support for intracellular partners involved in LTP signaling (Dupuis et al., 2014). Altogether, these pieces of evidence advocate for GluN2A-/GluN2B-NMDAR balance as a kingpin for adaptation at glutamatergic synapses. As the gross number of GluN2A and GluN2B-NMDAR in a hippocampal synapse of the CA1 area is in the range of 20-50 (Shinohara et al., 2008), our data suggest that the lateral redistribution of a limited fraction of NMDAR, as witnessed during LTP (Dupuis et al., 2014), is sufficient to alter the plastic range of a given synapse. Thus, fine tuning of GluN2A and GluN2B-NMDAR nano-organization at synapses emerges as a powerful regulator of neuronal network functions in the hippocampus.

ACKNOWLEDGMENTS

We thank the Bordeaux Imaging Center, a service unit of the CNRS-INSERM and Bordeaux University, member of the national infrastructure France BioImaging (ANR-10-INBS-04-01), specially C. Poujol and P. Mascalchi. We also thank Sebastian Malkusch and Mike Heilemann for support in DBSCAN analysis, Christophe Mulle for kindly providing the GluN2A$^{+/-}$ mice, Eric Gouaux for kindly providing antibody directed against the GluN1 subunit, the Plateforme de Biochimie Neurocentre Magendie, Pauline Durand for cell cultures and molecular biology, I. Gauthereau for technical assistance on protein expression, the Proteomic Platform of the Bordeaux Center for Functional Genomics (CGFB) for access to MALDI-TOF, and lab members for constructive discussions. This work was supported by the Erasmus Mundus Joint Doctorate (EMJD) program (European Neuroscience Campus), Programme d'Actions Universitaires Intégrés Luso-Françaises (2016/2017, 2017/2018), Centre National de la Recherche Scientifique, Agence Nationale de la Recherche (ANR-14-OHRI-0001-01, ANR-15-CE16-0004-03), IdEx Bordeaux (ANR-10-IDEX-03-02), Fondation pour la Recherche Médicale, Human Frontier Science Program (RGP0019), postdoctoral Marie-Curie Intra-European fellowship (neuroCHEMbiotools, #273817 to D.G-B), Conseil Régional d'Aquitaine, and Labex Bordeaux BRAIN, Wellcome Trust Principal Fellowship (101896/Z/13/Z).

REFERENCES

Al-Hallaq, R.A., Conrads, T.P., Veenstra, T.D., and Wenthold, R.J. (2007). NMDA di-heteromeric receptor populations and associated proteins in rat hippocampus. J Neurosci *27*, 8334-8343.

Bard, L., and Groc, L. (2011). Glutamate receptor dynamics and protein interaction: Lessons from the NMDA receptor. Mol Cell Neurosci *48(4)*, 298-307.

Bard, L., Sainlos, M., Bouchet, D., Cousins, S., Mikasova, L., Breillat, C., Stephenson, F.A., Imperiali, B., Choquet, D., and Groc, L. (2010). Dynamic and specific interaction between synaptic NR2-NMDA receptor and PDZ proteins. Proc Natl Acad Sci U S A *107*, 19561-19566.

Barth, A.L., and Malenka, R.C. (2001). NMDAR EPSC kinetics do not regulate the critical period for LTP at thalamocortical synapses. Nat Neurosci *4*, 235-236.

Bartlett, T.E., Bannister, N.J., Collett, V.J., Dargan, S.L., Massey, P.V., Bortolotto, Z.A., Fitzjohn, S.M., Bashir, Z.I., Collingridge, G.L., and Lodge, D. (2007). Differential roles of NR2A and NR2B-containing NMDA receptors in LTP and LTD in the CA1 region of two-week old rat hippocampus. Neuropharmacology *52*, 60-70.

Bayer, K.U., De Koninck, P., Leonard, A.S., Hell, J.W., and Schulman, H. (2001). Interaction with the NMDA receptor locks CaMKII in an active conformation. Nature *411*, 801-805.

Bellone, C., and Nicoll, R.A. (2007). Rapid bidirectional switching of synaptic NMDA receptors. Neuron *55*, 779-785.

Berberich, S., Punnakkal, P., Jensen, V., Pawlak, V., Seeburg, P.H., Hvalby, O., and Kohr, G. (2005). Lack of NMDA receptor subtype selectivity for hippocampal long-term potentiation. J Neurosci *25*, 6907-6910.

Bon, P., Linarès-Loyez, J., Feyeux, M., Alessandri, K., Lounis, B., Nassoy, P., and Cognet, L. (2018). Self-interference 3D super-resolution microscopy for deep tissue investigations Nature Methods *In Press*.

Broadhead, M.J., Horrocks, M.H., Zhu, F., Muresan, L., Benavides-Piccione, R., DeFelipe, J., Fricker, D., Kopanitsa, M.V., Duncan, R.R., Klenerman, D*., et al.* (2016). PSD95 nanoclusters are postsynaptic building blocks in hippocampus circuits. Sci Rep *6*, 24626.

Dudok, B., Barna, L., Ledri, M., Szabo, S.I., Szabadits, E., Pinter, B., Woodhams, S.G., Henstridge, C.M., Balla, G.Y., Nyilas, R*., et al.* (2015). Cell-specific STORM super-resolution imaging reveals nanoscale organization of cannabinoid signaling. Nat Neurosci *18*, 75-86.

Dupuis, J.P., Ladepeche, L., Seth, H., Bard, L., Varela, J., Mikasova, L., Bouchet, D., Rogemond, V., Honnorat, J., Hanse, E*., et al.* (2014). Surface dynamics of GluN2B-NMDA receptors controls plasticity of maturing glutamate synapses. EMBO J *33*, 842-861.

Ehmann, N., van de Linde, S., Alon, A., Ljaschenko, D., Keung, X.Z., Holm, T., Rings, A., DiAntonio, A., Hallermann, S., Ashery, U*., et al.* (2014). Quantitative super-resolution imaging of Bruchpilot distinguishes active zone states. Nat Commun *5*, 4650.

Fox, C.J., Russell, K.I., Wang, Y.T., and Christie, B.R. (2006). Contribution of NR2A and NR2B NMDA subunits to bidirectional synaptic plasticity in the hippocampus in vivo. Hippocampus *16*, 907-915.

Frank, R.A., Komiyama, N.H., Ryan, T.J., Zhu, F., O'Dell, T.J., and Grant, S.G. (2016). NMDA receptors are selectively partitioned into complexes and supercomplexes during synapse maturation. Nat Commun *7*, 11264.

Frost, N.A., Shroff, H., Kong, H., Betzig, E., and Blanpied, T.A. (2010). Single-molecule discrimination of discrete perisynaptic and distributed sites of actin filament assembly within dendritic spines. Neuron *67*, 86-99.

Garcia-Parajo, M.F., Cambi, A., Torreno-Pina, J.A., Thompson, N., and Jacobson, K. (2014). Nanoclustering as a dominant feature of plasma membrane organization. J Cell Sci *127*, 4995-5005.

Gardoni, F., Mauceri, D., Malinverno, M., Polli, F., Costa, C., Tozzi, A., Siliquini, S., Picconi, B., Cattabeni, F., Calabresi, P.*, et al.* (2009). Decreased NR2B subunit synaptic levels cause impaired long-term potentiation but not long-term depression. J Neurosci *29*, 669-677.

Godin, A.G., Lounis, B., and Cognet, L. (2014). Super-resolution microscopy approaches for live cell imaging. Biophys J *107*, 1777-1784.

Gray, J.A., Shi, Y., Usui, H., During, M.J., Sakimura, K., and Nicoll, R.A. (2011). Distinct modes of AMPA receptor suppression at developing synapses by GluN2A and GluN2B: single-cell NMDA receptor subunit deletion in vivo. Neuron *71*, 1085-1101.

Heilemann, M., van de Linde, S., Schuttpelz, M., Kasper, R., Seefeldt, B., Mukherjee, A., Tinnefeld, P., and Sauer, M. (2008). Subdiffraction-resolution fluorescence imaging with conventional fluorescent probes. Angew Chem Int Ed Engl *47*, 6172-6176.

Horak, M., Petralia, R.S., Kaniakova, M., and Sans, N. (2014). ER to synapse trafficking of NMDA receptors. Front Cell Neurosci *8*, 394.

Ito, I., Kawakami, R., Sakimura, K., Mishina, M., and Sugiyama, H. (2000). Input-specific targeting of NMDA receptor subtypes at mouse hippocampal CA3 pyramidal neuron synapses. Neuropharmacology *39*, 943-951.

Izumi, Y., Auberson, Y.P., and Zorumski, C.F. (2006). Zinc modulates bidirectional hippocampal plasticity by effects on NMDA receptors. J Neurosci *26*, 7181-7188.

Kawakami, R., Shinohara, Y., Kato, Y., Sugiyama, H., Shigemoto, R., and Ito, I. (2003). Asymmetrical allocation of NMDA receptor epsilon2 subunits in hippocampal circuitry. Science *300*, 990-994.

Lau, C.G., and Zukin, R.S. (2007). NMDA receptor trafficking in synaptic plasticity and neuropsychiatric disorders. Nat Rev Neurosci *8*, 413-426.

Levet, F., Hosy, E., Kechkar, A., Butler, C., Beghin, A., Choquet, D., and Sibarita, J.B. (2015). SR-Tesseler: a method to segment and quantify localization-based super-resolution microscopy data. Nat Methods *12*, 1065-1071.

Li, P., Banjade, S., Cheng, H.C., Kim, S., Chen, B., Guo, L., Llaguno, M., Hollingsworth, J.V., King, D.S., Banani, S.F.*, et al.* (2012). Phase transitions in the assembly of multivalent signalling proteins. Nature *483*, 336-340.

Li, R., Huang, F.S., Abbas, A.K., and Wigstrom, H. (2007). Role of NMDA receptor subtypes in different forms of NMDA-dependent synaptic plasticity. BMC Neurosci *8*, 55.

Lisman, J., Yasuda, R., and Raghavachari, S. (2012). Mechanisms of CaMKII action in long-term potentiation. Nat Rev Neurosci *13*, 169-182.

Liu, L., Wong, T.P., Pozza, M.F., Lingenhoehl, K., Wang, Y., Sheng, M., Auberson, Y.P., and Wang, Y.T. (2004). Role of NMDA receptor subtypes in governing the direction of hippocampal synaptic plasticity. Science *304*, 1021-1024.

Liu, Z., Lavis, L.D., and Betzig, E. (2015). Imaging live-cell dynamics and structure at the single-molecule level. Mol Cell *58*, 644-659.

Lu, W., Du, J., Goehring, A., and Gouaux, E. (2017). Cryo-EM structures of the triheteromeric NMDA receptor and its allosteric modulation. Science *355*.

Lussier, M.P., Sanz-Clemente, A., and Roche, K.W. (2015). Dynamic Regulation of N-Methyl-d-aspartate (NMDA) and alpha-Amino-3-hydroxy-5-methyl-4-isoxazolepropionic Acid (AMPA) Receptors by Posttranslational Modifications. J Biol Chem *290*, 28596-28603.

MacGillavry, H.D., Song, Y., Raghavachari, S., and Blanpied, T.A. (2013). Nanoscale scaffolding domains within the postsynaptic density concentrate synaptic AMPA receptors. Neuron *78*, 615-622.

Matta, J.A., Ashby, M.C., Sanz-Clemente, A., Roche, K.W., and Isaac, J.T. (2011). mGluR5 and NMDA receptors drive the experience- and activity-dependent NMDA receptor NR2B to NR2A subunit switch. Neuron *70*, 339-351.

Monyer, H., Burnashev, N., Laurie, D.J., Sakmann, B., and Seeburg, P.H. (1994). Developmental and regional expression in the rat brain and functional properties of four NMDA receptors. Neuron *12*, 529-540.

Nair, D., Hosy, E., Petersen, J.D., Constals, A., Giannone, G., Choquet, D., and Sibarita, J.B. (2013). Super-resolution imaging reveals that AMPA receptors inside synapses are dynamically organized in nanodomains regulated by PSD95. J Neuroscience *33*, 13204-13224.

Otmakhov, N., Tao-Cheng, J.H., Carpenter, S., Asrican, B., Dosemeci, A., Reese, T.S., and Lisman, J. (2004). Persistent accumulation of calcium/calmodulin-dependent protein kinase II in dendritic spines after induction of NMDA receptor-dependent chemical long-term potentiation. J Neurosci *24*, 9324-9331.

Paoletti, P., Bellone, C., and Zhou, Q. (2013). NMDA receptor subunit diversity: impact on receptor properties, synaptic plasticity and disease. Nat Rev Neurosci *14*, 383-400.

Park, C.S., Elgersma, Y., Grant, S.G., and Morrison, J.H. (2008). alpha-Isoform of calcium-calmodulin-dependent protein kinase II and postsynaptic density protein 95 differentially regulate synaptic expression of NR2A- and NR2B-containing N-methyl-d-aspartate receptors in hippocampus. Neuroscience *151*, 43-55.

Pennacchietti, F., Vascon, S., Nieus, T., Rosillo, C., Das, S., Tyagarajan, S.K., Diaspro, A., Del Bue, A., Petrini, E.M., Barberis, A*., et al.* (2017). Nanoscale Molecular Reorganization of the Inhibitory Postsynaptic Density Is a Determinant of GABAergic Synaptic Potentiation. J Neurosci *37*, 1747-1756.

Rauner, C., and Kohr, G. (2011). Triheteromeric NR1/NR2A/NR2B receptors constitute the major N-methyl-D-aspartate receptor population in adult hippocampal synapses. J Biol Chem *286*, 7558-7566.

Romberg, C., Raffel, J., Martin, L., Sprengel, R., Seeburg, P.H., Rawlins, J.N., Bannerman, D.M., and Paulsen, O. (2009). Induction and expression of GluA1 (GluR-A)-independent LTP in the hippocampus. Eur J Neurosci *29*, 1141-1152.

Sahl, S.J., Hell, S.W., and Jakobs, S. (2017). Fluorescence nanoscopy in cell biology. Nat Rev Mol Cell Biol *18*, 685-701.

Sainlos, M., Tigaret, C., Poujol, C., Olivier, N.B., Bard, L., Breillat, C., Thiolon, K., Choquet, D., and Imperiali, B. (2011). Biomimetic divalent ligands for the acute disruption of synaptic AMPAR stabilization. Nat Chem Biol *7*, 81-91.

Shinohara, Y., Hirase, H., Watanabe, M., Itakura, M., Takahashi, M., and Shigemoto, R. (2008). Left-right asymmetry of the hippocampal synapses with differential subunit allocation of glutamate receptors. Proc Natl Acad Sci U S A *105*, 19498-19503.

Shipton, O.A., and Paulsen, O. (2014). GluN2A and GluN2B subunit-containing NMDA receptors in hippocampal plasticity. Philos Trans R Soc Lond B Biol Sci *369*, 20130163.

Smith, G.B., Heynen, A.J., and Bear, M.F. (2009). Bidirectional synaptic mechanisms of ocular dominance plasticity in visual cortex. Philos Trans R Soc Lond B Biol Sci *364*, 357-367.

Specht, C.G., Izeddin, I., Rodriguez, P.C., El Beheiry, M., Rostaing, P., Darzacq, X., Dahan, M., and Triller, A. (2013). Quantitative nanoscopy of inhibitory synapses: counting gephyrin molecules and receptor binding sites. Neuron *79*, 308-321.

Tang, A.H., Chen, H., Li, T.P., Metzbower, S.R., MacGillavry, H.D., and Blanpied, T.A. (2016). A trans-synaptic nanocolumn aligns neurotransmitter release to receptors. Nature *536*, 210-214.

Volianskis, A., France, G., Jensen, M.S., Bortolotto, Z.A., Jane, D.E., and Collingridge, G.L. (2015). Long-term potentiation and the role of N-methyl-D-aspartate receptors. Brain Res *1621*, 5-16.

Yashiro, K., and Philpot, B.D. (2008). Regulation of NMDA receptor subunit expression and its implications for LTD, LTP, and metaplasticity. Neuropharmacology *55*, 1081-1094.

Zeng, M., Shang, Y., Araki, Y., Guo, T., Huganir, R.L., and Zhang, M. (2016). Phase Transition in Postsynaptic Densities Underlies Formation of Synaptic Complexes and Synaptic Plasticity. Cell *166*, 1163-1175 e1112.

Zhan, H., Stanciauskas, R., Stigloher, C., Dizon, K.K., Jospin, M., Bessereau, J.L., and Pinaud, F. (2014). In vivo single-molecule imaging identifies altered dynamics of calcium channels in dystrophin-mutant C. elegans. Nat Commun *5*, 4974.

Zhuang, X. (2009). Nano-imaging with Storm. Nat Photonics *3*, 365-367.

Figure legends

Figure 1. Nano-organization of GluN2A- and GluN2B-NMDAR in hippocampal neurons

A. Live immunostaining of endogenous surface GluN1 at DIV 17 labelled with a specific custom-made antibody. Upper panels: epifluorescence images of GluN1; left: dendritic shafts reveal a clustered distribution (scale bar = 10 µm); right: enlarged image of GluN1 clusters (scale bar = 500 nm). Lower panel: SR-Tesseler segmented GluN1 cluster.

B. Comparison between epifluorescence (left) and super-resolution dSTORM images generated by the Leica LAS software (right) of a single dendrite stained for either GluN2A- (top) or GluN2B-NMDAR (bottom). Dotted line represents the dendrite border based on the epifluorescence image. Scale bar = 1 µm.

C. Comparison of enlarged epifluorescence and dSTORM (generated by Leica LAS software) clusters of GluN2A- (top) or GluN2B-NMDAR (bottom). Dotted line represents the cluster border based on the epifluorescence image. Scale bar = 300 nm.

D. DBSCAN analysis of NMDAR clusters. Images of single GluN2A- and GluN2B-NMDAR clusters generated by LAMA software during DBSCAN analysis. Scale bar = 200 nm.

E. Differences in the area of super-resolved GluN2A- and GluN2B-NMDAR clusters represented by the mean ± SEM values (DBSCAN analysis).

F. Wavelet-based morphometric analysis (multi-dimensional image analysis, MIA) of NMDAR nanodomains. Enlarged single cluster of GluN2A- (left, blue) or GluN2B-NMDAR (right, orange), both composed of nanodomains. Images are representations of the MIA processing. Dotted line represents the outline of the epifluorescence cluster, arrows point to nanodomains within. Scale bar = 100 nm.

G. Comparison between GluN2A- and GluN2B-NMDAR nanodomains (MIA). Left: mean ± SEM values of GluN2A- and GluN2B-NMDAR nanodomain areas. Right: mean ± SEM values of the number of nanodomains per GluN2A- or GluN2B-NMDAR cluster.

H. SR-Tesseler analysis. Enlarged clusters of GluN2A- (top) and GluN2B-NMDAR generated by SR-Tesseler. Arrows point to nanodomains within the clusters. Scale bar = 100 nm.

I. Comparison between GluN2A- and GluN2B-NMDAR clusters and nanodomains using SR-Tesseler. Top: mean ± SEM values of GluN2A- and GluN2B-NMDAR cluster area. Bottom, left: mean ± SEM values of GluN2A- and GluN2B-NMDAR nanodomain areas, right: mean ± SEM values of GluN2A- and GluN2B-NMDAR nanodomain number per cluster. For statistical details refer to **Table S1**. For distribution representations see Figure S4.

Figure 2. Comparative nano-organization of GluN2A- and GluN2B-NMDAR within the same synaptic compartment

A. Schematic representation of experimental design. Hippocampal neurons were co-transfected with GluN1-GFP, GluN2A-HA and GluN2B-flag at DIV 10. The extracellularly expressed HA- and flag-tags were used to label GluN2A- and GluN2B-NMDAR, respectively, after 4 days of expression.

B. 2-color dSTORM image of GluN2A-HA (red) and GluN2B-flag (green). The dotted outline represents the outline of the GluN1-GFP epifluorescence cluster (lower inset; scale bar = 150 nm). Scale bar = 100 nm.

C. SR-Tesseler images of 2-color dSTORM of GluN2A-HA (magenta) and GluN2B-flag (green). *Right inset*, enlarged view of clusters in which the barycenters are indicated by dots. The red and green lines indicate the borders of GluN2A- and GluN2B-NMDAR nanodomains, respectively. Scale bar **=** 100 nm.

D. Percentage of colocalization between GluN2A-HA and GluN2B-flag represented by mean ± SEM values, obtained by SR-Tesseler.

Figure 3. Nanoscopic reorganization of GluN2A- and GluN2B-NMDAR during development

A. Images of enlarged clusters of GluN2A- (top) or GluN2B-NMDAR (bottom) during development of neuronal cultures. Images were generated by Lama software. Scale bar = 200 nm.

B. Changes in the cluster area of GluN2A- or GluN2B-NMDAR during development.

C. Developmental changes in the molecule number per GluN2A- and GluN2B-NMDAR cluster. Values are normalized to cluster area. For absolute numbers see **Table S2**.

D. Developmental changes in nanodomains within GluN2A- (top) and GluN2B-NMDAR (bottom) clusters (MIA). The dotted line represents the outline of respective epifluorescence clusters. Scale bar = 100 nm.

E. Developmental changes in the area of GluN2A- and GluN2B-NMDAR nanodomains.

F. Developmental changes in the number of nanodomains per cluster of GluN2A- or GluN2B-NMDAR. For statistical details refer to **Table S1**.

Figure 4. Selective reorganization of GluN2A- and GluN2B-NMDAR using biomimetic ligands

A-B. Effects of TAT-conjugated competing ligands on GluN2A- and GluN2B-NMDAR surface trafficking within synapses. **A.** Single nanoparticle (Quantum Dot) trajectories of GluN2A- and GluN2B-NMDAR in presence of either TAT-NS_2, TAT-$2A_2$, or TAT-$2B_2$ ligands (mimicking the last 15 amino acids of either GluN2A or GluN2B subunit C-termini). The synaptic area was defined by Mitotracker staining (see STAR Methods). Scale bar = 150 nm.

B. Percent change in instantaneous synaptic diffusion coefficients of GluN2A- and GluN2B-QD complexes exposed to either TAT-NS_2, TAT-$2A_2$, or TAT-$2B_2$ ligands. The values are expressed as percent of variation to the TAT-NS_2 condition.

C. Top panel: enlarged GluN2A-NMDAR cluster (Lama) following stimulation with either TAT-NS_2 or specific TAT-$2A_2$ ligands. Scale bar = 200 nm. Bottom panel: mean ± SEM values of GluN2A-NMDAR cluster area and molecule number per cluster in control and TAT-$2A_2$ ligand conditions. Values are normalized to TAT-NS_2.

D. Top panel: GluN2A-NMDAR nanodomains (MIA) following treatment with either TAT-NS_2 or specific TAT-$2A_2$ ligands. Dotted line represents the outline of respective epifluorescence clusters. Scale bar = 200 nm. Bottom panel: mean ± SEM values of GluN2A-NMDAR nanodomain area and number per cluster.

E. Top panel: enlarged GluN2B-NMDAR cluster (Lama) following stimulation with either TAT-NS_2 or specific TAT-$2B_2$ ligands. Scale bar = 200 nm. Bottom panel: mean ± SEM values of GluN2B-NMDAR cluster area and molecule number per cluster in control and TAT-$2B_2$ conditions. Values are normalized to TAT-NS_2.

F. Top panel: GluN2B-NMDAR nanodomains (MIA) following treatment with either TAT-NS_2 or specific TAT-$2B_2$ ligands. Dotted line represents the outline of respective epifluorescence clusters. Scale bar = 200 nm. Bottom panel: mean ± SEM values of GluN2B-NMDAR nanodomain area and number per cluster.

Scale bar = 200 nm. For statistical details refer to **Table S1**.

Figure 5. Selective disruption of the interaction between GluN2A- or GluN2B-NMDARs and PDZ proteins allows acute manipulation of the composition of synaptic NMDAR

A. Representative NMDAR-mediated EPSC traces recorded at CA3-CA1 synapses from P17 to P22 C57bl6j mice before and after incubation with Ro 25-6981 (2 µM) in the presence of either non-sense (NS_2; black), GluN2A-selective ($2A_2$; blue) or GluN2B-selective ($2B_2$; orange) competing ligands (5 µM) infused through the patch pipette.

B. NMDAR-mediated EPSC amplitude before and after incubation with Ro 25-6981 (2 µM) in the presence of NS_2 non-sense ligand.

C. Relative NMDAR-mediated EPSC amplitude after 20 minute incubation with Ro 25-6981 (2 µM) in the absence or presence of non-sense (NS_2; black), GluN2A-selective ($2A_2$; blue) or GluN2B-selective ($2B_2$; orange) competing ligands (5 µM) infused through the patch pipette.

D. Representative NMDAR-mediated EPSC traces recorded at CA3-CA1 synapses from P17 to P22 C57bl6j mice before and after incubation with Zn^{2+} (250 nM) in the presence of either non-sense (NS_2; black), GluN2A-selective ($2A_2$; blue) or GluN2B-selective ($2B_2$; orange) competing ligands (5 µM) infused through the patch pipette.

E. NMDAR-mediated EPSC amplitude before and after incubation with Zn^{2+} (250 nM) in the presence of NS_2 non-sense ligand.

F. Relative NMDAR-mediated EPSC amplitude after 20 minute incubation with Zn^{2+} (250 nM) in the absence or presence of non-sense (NS_2; black), GluN2A-selective ($2A_2$; blue) or GluN2B-selective ($2B_2$; orange) competing ligands (5 µM) infused through the patch pipette.

G. NMDAR-mediated EPSC amplitude 5 min and 20 min after incubation with NS_2 non-sense ligand.

H. Relative NMDAR-mediated EPSC amplitude after a 20 minute exposure to non-sense (NS_2; black), GluN2A-selective ($2A_2$; blue) or GluN2B-selective ($2B_2$; orange) competing ligands (5 µM) infused through the patch pipette.

Figure 6. Acute manipulation of the GluN2A/GluN2B-NMDAR synaptic ratio bi-directionally regulates LTP at CA3-CA1 synapses

A. Representative EPSC traces recorded at CA3-CA1 synapses from P17 to P22 C57bl6j mice during baseline (grey) or 40-45 min after pairing in the presence of either non-sense (NS_2; black), GluN2A-selective ($2A_2$; blue) or GluN2B-selective ($2B_2$; orange) competing ligands (5 µM) infused through the patch pipette.

B. Average time course of pairing-induced LTP. Normalized EPSC amplitudes (normalization to the mean amplitude of EPSCs recorded during baseline acquisition) are plotted against time for non-sense (NS_2; black), GluN2A-selective ($2A_2$; blue), and GluN2B-selective ($2B_2$; orange) competing ligands conditions. Data are presented as mean ± SEM.

C. Normalized EPSC amplitudes at baseline or 40 - 45 min after pairing in non-sense (NS_2; black), non-sense + AP5 50 µM (NS_2 + AP5; white), GluN2A-selective ($2A_2$; blue), and GluN2B-selective ($2B_2$; orange) competing ligands conditions. Data are presented as mean ± SEM. Preventing the synaptic stabilization of GluN2A-NMDAR increased the plastic range of hippocampal synapses while preventing the synaptic stabilization of GluN2B-NMDAR decreased it.

D. In basal condition, GluN2A- and GluN2B-NMDAR are organized in nanodomains (GluN2A > GluN2B). After disrupting the interaction between C-termini and PDZ scaffolds, GluN2A- and GluN2B-NMDAR nanodomains are re-organized through two distinct modes: the number of GluN2A-NMDAR is altered in a fixed domain, whereas the number of GluN2B-NMDAR remains unchanged in an altered 'labile' domain. These manipulations lead to opposite changes in LTP at CA3-CA1 synapses.

Supplementary Figure 1. Characterization of custom-made anti-GluN2A and anti-GluN2B antibodies

A. Schematic of the workflow for immunocytochemical validation of antibody specificity. COS7 cells were electroporated with GluN1-SEP plus GluN2A-HA or GluN2B-flag. They were then fixed and labelled with either custom-made anti-GluN2A, custom-made anti-GluN2B, anti-HA or anti-flag.

B. Representative images of electroporated COS7 cells specifically labelled for the GluN2 subunit or the plasmid tag (Red). Small panels (green) correspond to GluN1-SEP fluorescence. DAPI mounting medium was used for cell identification (blue). Non-transfected cells were used as control. Scale bar = 50 µM.

C. Schematic of the workflow for biochemical validation of antibody specificity (top). Non-transfected COS cells, COS cells electroporated either with GluN2A/GluN1 or GluN2B/GluN1, lysates obtained from GluN2A$^{+/+}$ or GluN2A$^{-/-}$ mice brains (P15) or cultured neurons from GluN2B$^{+/+}$ or GluN2B$^{-/-}$ mice were analyzed by western-blot using the specific custom-made GluN2A or GluN2B antibodies. Actin was used as the loading control.

Specific labeling was observed for the two antibodies and no cross-reactivity with the other subunit was observed.

Supplementary Figure 2. Development of hippocampal cultures

A. Representative epifluorescence images of surface GluN2A- (left) or GluN2B-NMDAR (right) in neuronal cultures at DIV 17. Scale bar = 10 µm.

B. Representative epifluorescence images of surface GluN2A- (left) or GluN2B-NMDAR (right) in neuronal cultures at DIV 10 (top), 17 (middle) or 24 (bottom). Scale bar = 2 µm.

C. Bar graphs representing changes in surface expression of NMDAR (linear density of GluN2A or GluN2B clusters per 10 µm dendrite length) during development, represented as mean ± SEM values.

D. Representative epifluorescence images of PSD95 (left) or VGLUT (right) in neuronal cultures at DIV 10 (top), 17 (middle) or 24 (bottom). Scale bar = 5 µm.

E. Bar graphs representing the changes in PSD95 expression during development. Left, linear density of PSD95 clusters per 10 µm dendrite length. Right: PSD95 cluster area.

For statistical details refer to **Table S1**.

Supplementary Figure 3. Localization precision

Localization precision of GluN2A- (**A**) and GluN2B-NMDAR (**B**) immunostained with specific primary antibodies and secondary antibodies conjugated with AlexaFluor 647, according to Thompson (black) and Mortensen (gray) (mean ± SEM).

For statistical details refer to **Table S1**.

Supplementary Figure 4. Distributions of GluN2A- and GluN2B-NMDAR clusters and nanodomains in mature neurons

A. Frequency distributions of the areas of super-resolved GluN2A- and GluN2B-NMDAR clusters based on DBSCAN analysis.

B-E. Wavelet-based morphometric analysis of NMDAR clusters and nanodomains. **B.** Frequency distributions of GluN2A- and GluN2B-NMDAR nanodomain area. **C.** Frequency distributions of the number of nanodomains contained within GluN2A- or GluN2B-NMDAR clusters. **D.** Comparison between GluN2A- and GluN2B-NMDAR nanodomain shape factors. **E.** Differences in the cluster area of GluN2A- and GluN2B-NMDAR represented by mean ± SEM (left) and their frequency distribution (right).

F-H. SR-Tesseler-based analysis of NMDAR clusters and nanodomains. Frequency distributions of GluN2A- and GluN2B-NMDAR cluster area (**F**), nanodomain area (**G**) and nanodomain number per cluster (**H**).

For statistical details refer to **Table S1**.

Supplementary Figure 5. Comparison of 2D and 3D-SELFI-dSTORM of GluN2A- and GluN2B-NMDAR

A. 3D-SELFI-dSTORM of GluN2B-NMDAR: representative image of quasi-isotropic 3D dSTORM reconstruction of an NMDAR cluster using SELFI, and respective projections in xy, yz and zx (2D), according to their different localization precisions (e.g. for 1000 detected photons/molecule: σ_{xy} ~ 5 nm, σ_z ~ 10 nm). Dotted red lines highlight the difference in identifiable nanodomains when only a single xy, yz or zx projection is taken into consideration. Color scale z: -50-65 nm. Image was generated using a homemade LABVIEW software.

B. Bar graph of mean ± SEM values of the number of nanodomains in GluN2A- and GluN2B-NMDAR clusters in 3D-reconstruction.

C. Paired-analysis of the counting of nanodomains in the xy 2D-projection compared to the 3D projection of the same selected GluN2 subunit cluster.

For statistical details refer to **Table S1**.

Supplementary Figure 6. Linear density of GluN1 and its colocalization with pre- and postsynaptic proteins

A. Representative epifluorescence images of DIV 14 neurons with surface labelling of overexpressed GluN1-SEP, endogenous PSD95 or endogenous VGLUT and their overlap (green: GluN1-SEP 19.5 ± 1.3, red: PSD95 11.9 ± 0.9, blue: VGLUT 18.1 ± 1.1 clusters per 10 µm of dendrite represented as mean ± SEM). Scale bar = 10 µM.

B. Number of clusters (left) or colocalizing clusters (right) per 10 µm dendrite length.

Supplementary Figure 7. Comparison of PSD95-positive (PSD95+) GluN2A- and GluN2B-NMDAR clusters in mature neurons

A. dSTORM image (Leica LAS software) of GluN2A- (left, green) or GluN2B-NMDAR (right, green) overlaid with the corresponding epifluorescence image of PSD95 (red) at DIV 17. Dotted line represents the border of the dendrite based on the NMDAR epifluorescence image. Full arrowheads

point to PSD95 positive (PSD95+) NMDAR clusters, while open arrowheads point to PSD95 negative (PSD95-) NMDAR clusters. Scale bar = 2 µm.

B. Ratio of PSD95+ GluN2A- and GluN2B-NMDAR over total surface clusters represented by mean ± SEM values.

C. Left, enlarged epifluorescence PSD95 clusters with dotted outline. Right, enlarged PSD95+ GluN2A- (top) or GluN2B-NMDAR (bottom) cluster. Scale bar = 300 nm.

D. Differences in the area of PSD95+ GluN2A- and PSD95+ GluN2B-NMDAR clusters represented by the mean ± SEM values (left) and frequency distributions (right).

E-G. Comparison between PSD95-positive (PSD95+) GluN2A- and GluN2B-NMDAR nanodomains. **E.** Representative images of MIA-processed PSD95+ GluN2A- (top) and GluN2B-NMDAR (bottom) nanodomains. Scale bar = 200 nm. **F.** Bar graph (left) and frequency distributions (right) of PSD95+ nanodomain area. **G.** Bar graph (left; mean ± SEM values) and frequency distributions (right) of GluN2A- or GluN2B-NMDAR nanodomain numbers per PSD95+ cluster.

For statistical details refer to **Table S1**.

Supplementary Figure 8. Comparison of over-expressed GluN2A- and GluN2B-NMDAR staining using confocal microscopy

Representative confocal microscopy image of a cluster of overexpressed GluN2A-HA – AlexaFluor 594 (left), GluN2B-flag – Atto647N (middle), and the merge of the two (right; magenta: GluN2A, green: GluN2B-flag). The red dotted line represents the outline of the spine morphology obtained from GluN1-GFP expression. Scale bar = 400 nm.

Supplementary Figure 9. STED imaging of NMDAR clusters on hippocampal neurons

A. Example of NMDAR cluster observed in STED microscopy on hippocampal neurons expressing both GluN2A-HA and GluN2B-flag (right; magenta: GluN2A, green: GluN2B). Scale bar = 400 nm.

B. Paired analysis of GluN2A-HA and GluN2B-flag cluster areas within a same synapse.

C. Fraction of GluN2A clusters that colocalize with GluN2B clusters.

For statistical details refer to **Table S1**.

Supplementary Figure 10. Divalent ligand design and characterization

A. Design and sequences of 2A- and 2B-derived divalent ligands. C-terminal parts of the 2A- or 2B-containing NMDAR mimicked by the biomimetic divalent ligands (right) are highlighted with a blue circle.

B. Binding properties of ligands. Competitive titration curves were obtained by successively adding a non-fluorescent ligand to a mixture of PSD-95 first two PDZ domains in the presence of a fluorescence probe derived from 2A15 peptide and labelled with the environment sensitive fluorophore 4-DMAP at position -5. The X axis represents the total concentration of added non-fluorescent ligand. Error bars represent the standard deviation (n > 2). The KI values obtained for each ligands were the following ($K_I \pm$ s.d.): $2A_{15}$ 7.28 $\pm$ 0.20 μM; $2B_{15}$ 16.34 $\pm$ 0.98 μM; $[2A_{15}]_2$ 0.18 $\pm$ 0.02 μM; $[2B_{15}]_2$ 0.26 $\pm$ 0.02 μM. The inset plot represents the direct titration of the fluorescent probe with PSD-95 first two PDZ domains (K_D 1.58 $\pm$ 0.20 μM). Error bars represent the standard deviation (n > 2).

Supplementary Figure 11. Peptide-based ligand sequences and characterization

A. Summary table for properties of the synthesized ligands used in this study. ϕ: Dab(4-DMAP). λ: Norleucine. Ac-: acetyl group. Entry 1 corresponds to a monomeric peptide labelled with an environment sensitive fluorophore (4-DMAP) at position -5 used in direct titration experiments. Entries 2-3 correspond to monovalent ligands. Entry 4 corresponds to a non-sense sequence derived from Stargazin ligand. A Y residue is introduced at N-terminus for quantification purposes. Entries 4-6 correspond to divalent ligands. tR: retention time expressed in minutes. Purity was assessed by analytical reverse phase HPLC (YMC C18, ODS-A 5/120, 250×4.6 mm) using a standard gradient (5 % acetonitrile containing 0.1 % TFA for 5 min followed by 5-95 % acetonitrile containing 0.1 % TFA over

50 min in water containing 0.1 % TFA at a flow rate of 1 mL.min-1). All of the peptide-based ligands were more than 90 % pure as judged by analytical HPLC. The identity of the peptide-based ligands was confirmed by MALDI-TOF mass spectroscopy using an UltraFlex III TOF-TOF (Bruker Daltonics, Bremen, Germany) with DHB or ACH as a matrix in a reflector mode. The observed masses are consistent with the calculated masses of the desired products.

B. Structure of the ligands used in this study.

Supplementary Figure 12. Divalent ligand synthesis scheme

Steps followed to obtain divalent ligands, either acetylated (compounds **4-6**) or labelled with the TAT cell-penetrating sequence (compounds **7-9**) at the N-terminus. The inset (top right) represents the synthetic steps followed to obtain the Ac-Lys(N_3)-TAT-OH sequence that can be coupled to a divalent ligand by using copper-catalyzed azide–alkyne click chemistry in solution. [a] Nova syn TGA resin to generate free carboxylic acid at the C-terminus of the peptides. [b] PAL-NOVA-PEG resin to generate amide groups at the C-terminus of the peptide. [c] A mixture 7: 3.5 of an azide (Fmoc-Lys(N_3)-OH) and an alkyne (Pentynoic acid) is used in order to prepare the peptides to be dimerized by on-resin by copper-catalyzed azide–alkyne click chemistry [d] on resin ligation is achieved by means of an overnight copper-catalyzed azide–alkyne click chemistry reaction using 5 eq. of CuI and 5 eq. of ascorbic acid in 20 % piperidine in DMF. [e] ligation of the TAT sequence to divalent ligands is performed in solution in 200 mM phosphate buffer pH 8 [f] The reaction is dissolved in the starting solvent for HPLC purification (H_20 containing 0.1% TFA).

Supplementary Figure 13. Changes in molecule density after TAT ligand treatment

A. Distributions of GluN2A density: molecule number per nanodomain area after exposure to TAT-NS_2 or TAT-$2A_2$.

B. Distributions of GluN2B density: molecule number per nanodomain area after exposure to TAT-NS_2 or TAT-$2B_2$.

For statistical details refer to **Table S1**. For absolute molecule number see **Table S2**.

Supplementary Figure 14. Crossed impacts of TAT ligands on GluN2A and GluN2B surface clusters

A. Evolution of a GluN2B-NMDAR cluster (Lama) following treatment with either TAT-NS_2 or TAT-$2A_2$ ligands.

B. Evolution of GluN2B-NMDAR cluster areas and cluster molecule numbers in TAT-NS_2 and TAT-$2A_2$ conditions. Values are normalized to TAT-NS_2 (mean ± SEM).

C. Evolution of GluN2B-NMDAR nanodomains (MIA) following treatment with either TAT-NS_2 or TAT-$2A_2$ ligands.

D. Evolution of GluN2B-NMDAR nanodomain areas and numbers in TAT-NS_2 and TAT-$2A_2$ conditions. Values are normalized to TAT-NS_2 (mean ± SEM).

E. Evolution of a GluN2A-NMDAR cluster (Lama) following treatment with either TAT-NS_2 or TAT-$2B_2$ ligands.

F. Evolution of GluN2A-NMDAR cluster areas and cluster molecule numbers in TAT-NS_2 and TAT-$2B_2$ conditions. Values are normalized to TAT-NS_2 (mean ± SEM).

G. Evolution of GluN2A-NMDAR nanodomains (MIA) following treatment with either TAT-NS_2 or TAT-$2B_2$ ligand.

H. Evolution of GluN2A-NMDAR nanodomain areas and numbers in TAT-NS_2 and TAT-$2B_2$ conditions. Values are normalized to TAT-NS_2 (mean ± SEM).

Scale bars = 200 nm. For statistical details refer to **Table S1**. For absolute molecule number see **Table S2**.

Figure 1

Kellermayer, Ferreira, Dupuis et al.

worth saying if this is confocal or wide-field

maybe 'molecular density'?

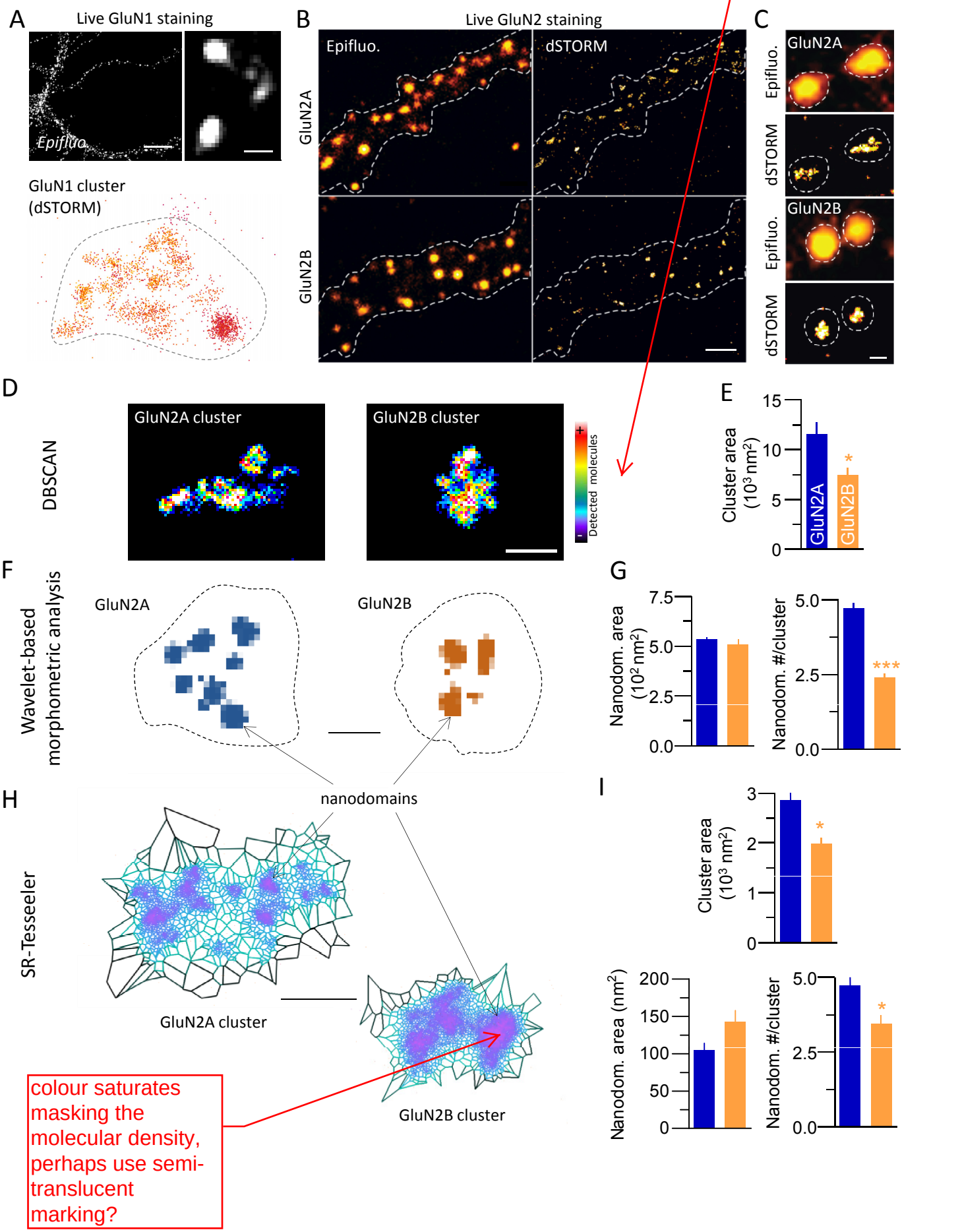

colour saturates masking the molecular density, perhaps use semi-translucent marking?

Figure 2

Kellermayer, Ferreira, Dupuis et al.

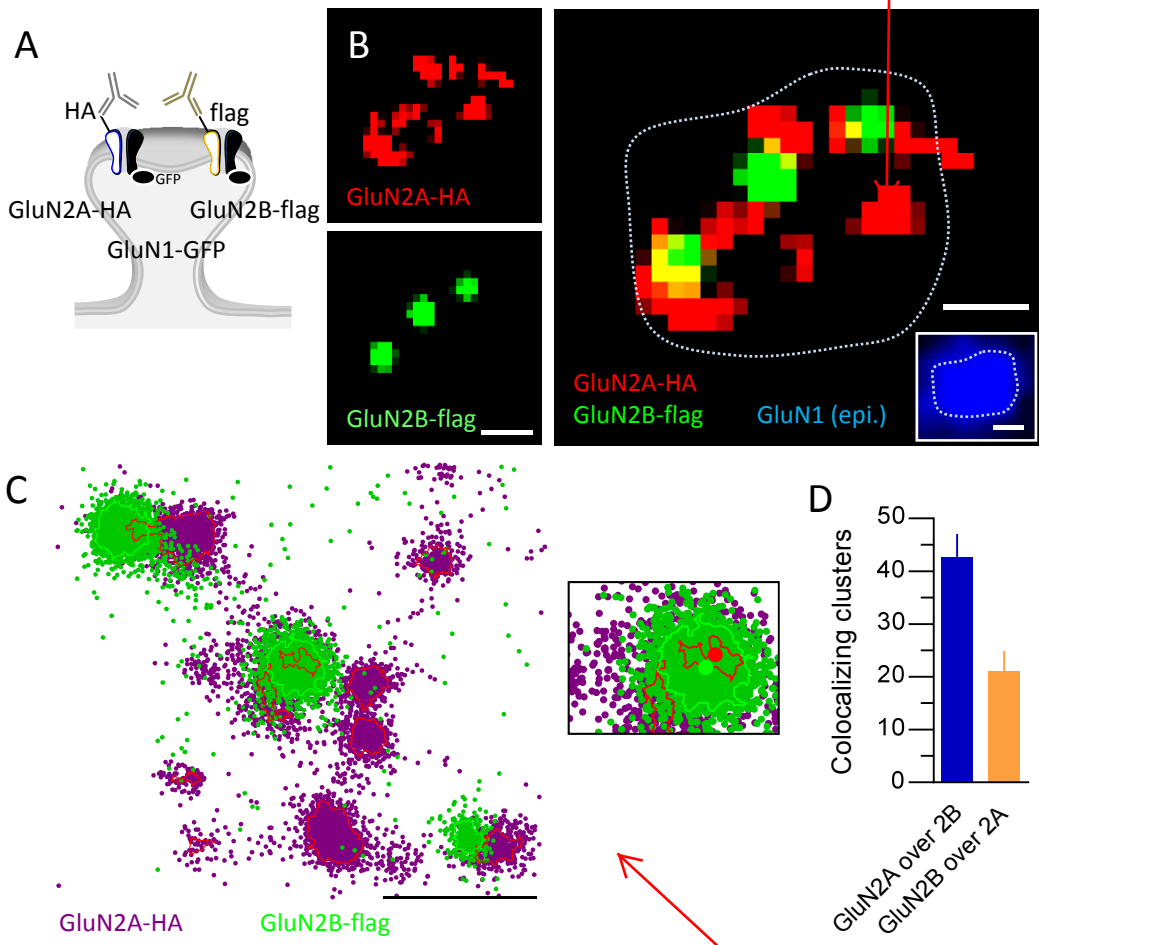

Figure 3

Kellermayer, Ferreira, Dupuis et al.

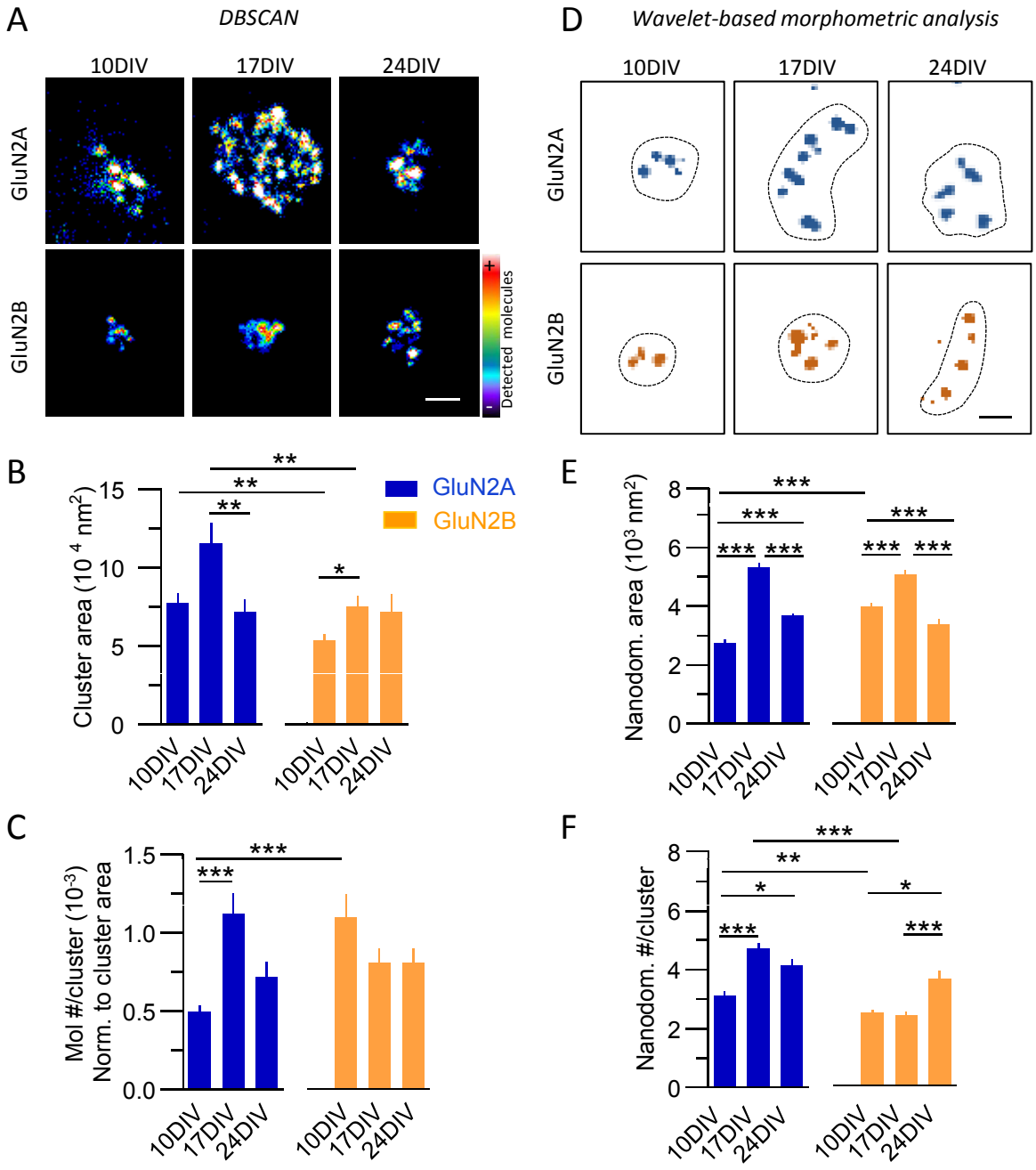

Figure 4

Kellermayer, Ferreira, Dupuis et al.

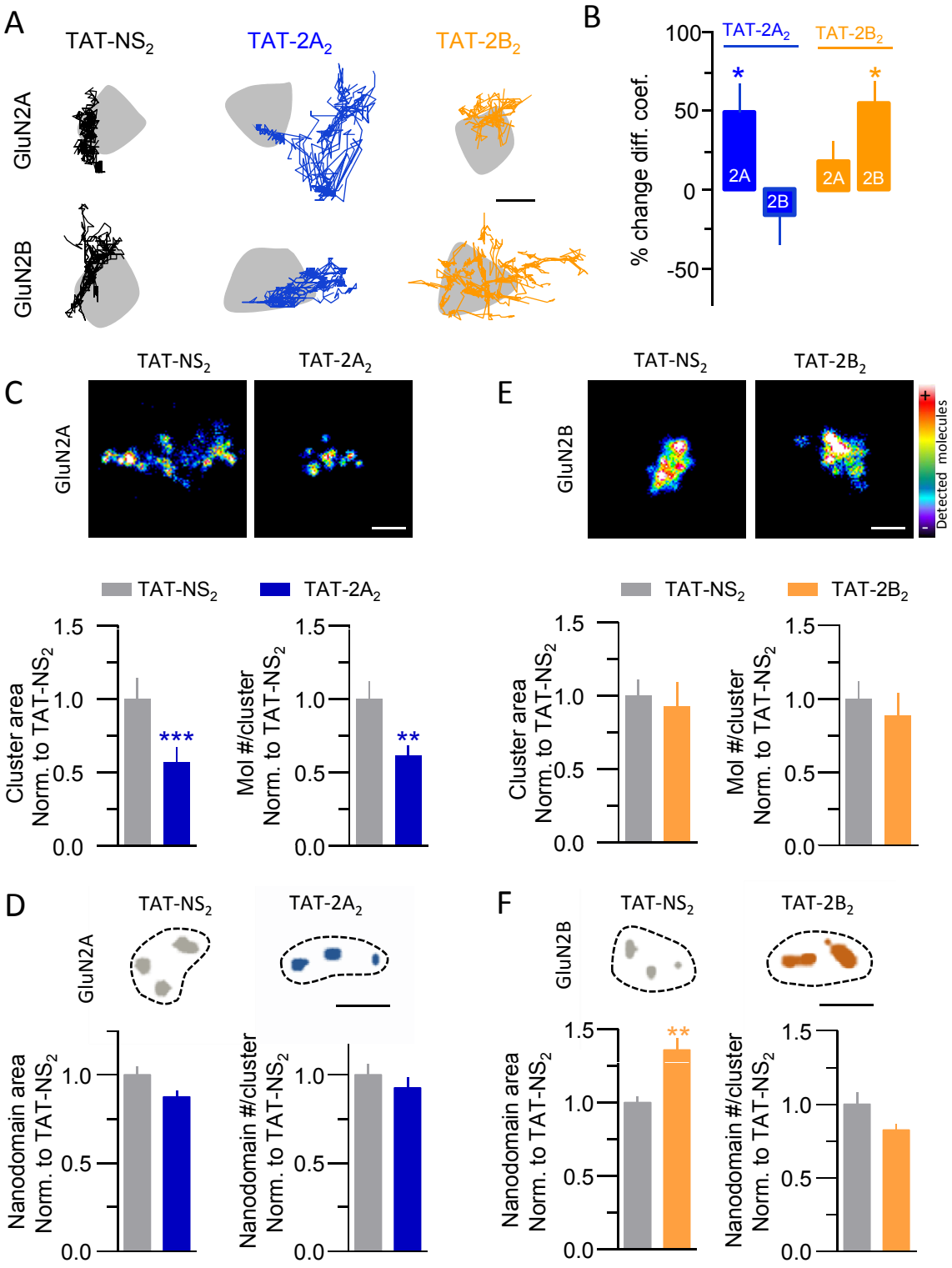

Figure 5

Kellermayer, Ferreira, Dupuis et al.

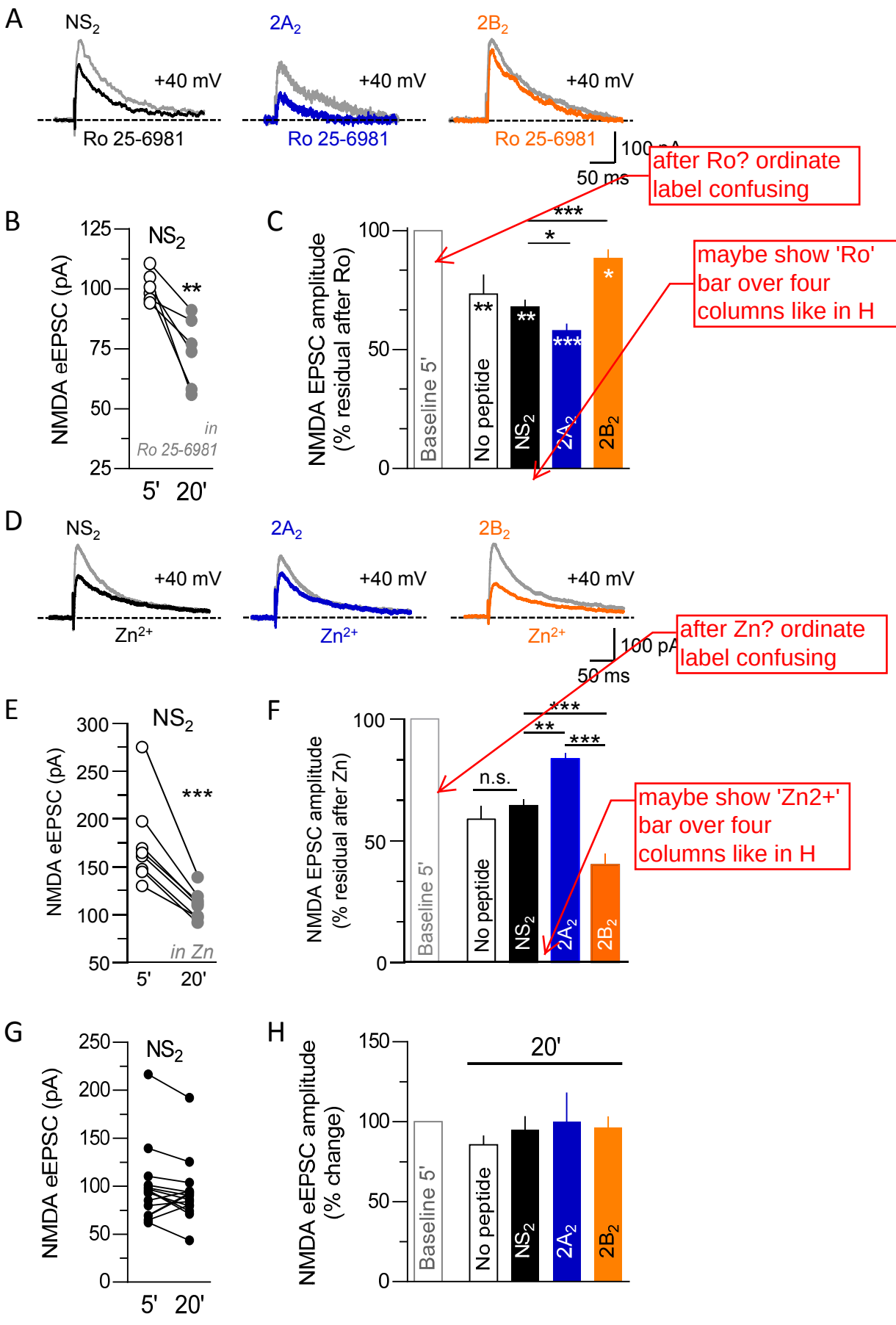

Figure 6

Kellermayer, Ferreira, Dupuis et al.

show 'LTP' over four columns, otherwise looks like effect of pharmacology only